Tilt-induced kink in the plasmon dispersion of two-dimensional Dirac electrons

Z. Jalali-Mola[1,*] and S. A. Jafari[1,2,†]

[1]*Department of Physics, Sharif University of Technology, Tehran 11155-9161, Iran*

[2]*School of Physics, Institute for Research in Fundamental Sciences (IPM), Tehran 19395-5531, Iran*

(Received 24 July 2018; revised manuscript received 30 August 2018; published 12 November 2018)

The list of two-dimensional Dirac systems with a tilt in their Dirac cone spectrum is expanding, and now, in addition to the organic system α(BEDT-TTF)$_2$I$_3$, it includes the two-dimensional 8$Pmmn$-borophene sheet, which allows for controlled doping by the gate voltage. We analytically calculate the polarization function of tilted Dirac cone for an arbitrary tilt parameter, $0 \leqslant \eta < 1$, and arbitrary doping. This enables us to find two interesting plasmonic effects solely caused by the tilt. (i) In addition to the standard plasmon oscillations, a strong enough tilt induces an additional linearly dispersing overdamped branch of plasmons, which is strongly Landau damped due to overlap with a large density of intraband free particle-hole (PH) excitations. (ii) There appears a kink in the plasmon dispersion for any nonzero tilt parameter. The kink appears when the plasmon branch enters the interband continuum of PH excitations. This kink becomes most manifest for wave vectors perpendicular to the tilt direction and fades away by approaching the tilt direction. Experimental measurements of the wave vector and energy of the plasmonic kink, when combined with our analytic formula for the kink energy scale, allow for a direct experimental estimation of the tilt parameter. Furthermore, we find that, for a fixed chemical potential μ, the screening is significantly enhanced by bringing the tilt η close to 1.

DOI: 10.1103/PhysRevB.98.195415

I. INTRODUCTION

Dirac materials are now quite ubiquitous in condensed matter physics [1], and include one [2], two [3], and three spatial dimensions [1,4,5]. In two dimensions, a well-known example of Dirac material is graphene [6–8], the two-dimensional character of which allows for functionalization [9] and various manipulations. The interesting thing about condensed-matter Dirac systems is that—unlike in high-energy physics—they can be deformed in many ways. The lattice distortion can induce anisotropy in the velocity v_x, v_y [10], or can reshape the Brillouin zone, which then moves the Dirac cones in the k space [11]. One particularly interesting deformation of the Dirac cone is to tilt it. In the case of graphene, a very small amount of tilting can be achieved through coupling to lattice deformations [12]. The first example of substantial tilt in the Dirac cone was, however, realized in the molecular organic material α-(BEDT-TTF)$_2$I$_3$ [13,14]. The smaller velocity scales of molecular orbitals compared to atomic p_z orbitals of graphene makes the tilt perturbation quite large in these systems [13,15,16].

The layered organic conductor α-(BEDT-TTF)$_2$I$_3$, is one of 2D Dirac cone materials, which consists of conducting layers of BEDT-TTF molecules separated by insulating layers of I_3^- anions, where conduction electrons are arranged on the square lattice with four molecules BEDT-TTF per unit cell [15]. As the layers are weakly coupled to each other, the material under hydrostatic pressure above 1.5 GPa is a quasi-two-dimensional zero-gap conductor with linear dispersion. However, the major difference between the zero-gap state of an organic conductor with the well-known graphene is that the graphene dispersion is rotationally invariant along the axis of the Dirac cone, but a single tilted Dirac cone is not rotationally invariant along the z axis. Moreover, the cone axis is not normal to the $\boldsymbol{k}$ plane and a tilt parameter $0 \leqslant \eta < 1$ quantifies how much the Dirac cone is tilted along a direction determined by an angle θ_t in the (k_x, k_y) plane. In addition, unlike graphene, where the two Dirac cones are located at K and K', in an organic conductor, the Dirac cones are located at general points $\pm\boldsymbol{k}_0$ with opposite tilting direction. Electronic structure calculations suggest anisotropic velocities $v_x, v_y \sim 10^5$m/s [15,17–19]. The empirically determined velocities are slightly less than these values [15]. The tilted anisotropic Dirac equation that describes the low energy band structure in this system has been confirmed by *ab initio* calculations [13,15,20–23].

As pointed out, the tilting can be induced in graphene by coupling to the lattice deformation, which is accompanied by rotation symmetry breaking [12,24]. However, this way of tilting the Dirac cone is more difficult and gives rise to a small tilt. However, elemental boron—just to the left of carbon in the periodic table—can also afford to form a two-dimensional allotrope [25]. The stable structure of borophene is the so-called orthorhombic 8-$Pmmn$. This structure with two nonequivalent buckled sublattices [26], possesses a tilted anisotropic Dirac cone, which has been suggested by *ab initio* calculations [26–28]. The borophene is now synthesized on Ag(111) surface and features an anisotropic Dirac cone [29]. In this material, the velocities are $(v_x, v_y) \simeq (0.86, 0.69) \times 10^6$m/s [30]. Therefore the kinetic energy scale of Dirac electrons in borophene is slightly less than graphene. The tilted Dirac dispersion in borophene holds in energy scales of $\sim$1 eV. In organic materials, the kinetic energy is at least an order of magnitude smaller than the kinetic energy of Dirac

*jalali@physics.sharif.edu
†jafari@physics.sharif.edu

electrons in graphene, and is on the scale of 70 meV [16]. This already signals that the many-body fluctuation phenomena in tilted Dirac cone materials must be even more profound than in graphene [31].

The two-dimensionality of the latest 8-$Pmmn$ borophene allows for controlled doping by the gate voltage. Therefore it is timely to investigate the collective excitations of this system. For this, one needs an analytical understanding of the polarization function that describes the density-density correlations in the system. This fundamental quantity has been thoroughly calculated for the up-right Dirac cone in graphene [32,33]. In the case of a tilted Dirac cone, Nishine and coworkers have given an analytical formula for the imaginary part of the polarization function [34]. The real part in their work is numerically calculated via the Kramers-Kronig relation from the imaginary part [34]. In a recent work, Sadhukhan and Agarwal have attempted to give an analytical calculation of the polarization function. However, the determination of the signs and Fermi step functions in their work has not been correctly accomplished [35]. The above two works do not agree with each other. In this work, as will be detailed in the appendices, we meticulously calculate the polarization function for a tilted Dirac cone, and obtain the analytical representation of both real and imaginary parts of it for arbitrary doping. Our results agree with the numerical results of Ref. [34] for the real part.

Our analytical result allows for a detailed study of the plasmon excitations per valley in tilted Dirac cone systems. First of all, we find that, when the standard plasmon branch enters the interband portion of the PH continuum (PHC), it develops a kink. Again, our analytic formula enables us to show that the Landau damping in the interband PHC is negligible. Therefore the plasmon branch on both sides of the kink will be long-lived, and can be experimentally determined. The entire plasmon structure is anisotropic, and the kink is most manifest for wave vectors perpendicular to the tilt direction. We suggest that a knowledge of the wave vector and frequency of the kink, in hindsight, can be used for direct determination of the tilt parameter from angular resolved electron energy loss spectroscopy (EELS) [36]. Our analytic formula further enables us to find that for large enough tilt parameters, another branch of linearly dispersing plasmon excitations exists inside the intraband PHC, which is overdamped due to a very large density of states (DOS) of PH excitations.

This paper is organized as follows. In Sec. II, we formalize the tilt and derive our analytic representation of the polarization function. In Sec. III, we give a qualitative discussion of the role of tilt in plasmonic properties. In Sec. IV, we identify the kink in the plasmon dispersion and explain the physics behind it and suggest it as a way to experimentally measure the tilt. In Sec. V, we provide an asymptotic formula to address plasmons and static screening in the presence of kink. In the appendices we give the details of the calculation to enable the reader to re-derive our results. We end the paper with the summary of our findings.

II. TILTED DIRAC CONE MODEL

An effective theory of massless tilted Dirac fermions is given by the following deformation of the Dirac equation [16,34]:

$$H(k)=\hbar\begin{pmatrix} v_{x0}k_x+v_{y0}k_y & v_xk_x-iv_yk_y \\ v_xk_x+iv_yk_y & v_{x0}k_x+v_{y0}k_y\end{pmatrix}, \tag{1}$$

where the off-diagonal (Fermi) velocities v_x and v_y are different, and stand for anisotropy, and the diagonal velocities v_{x0} and v_{y0} represent the tilting characteristic of the system. If we consider $v_{x0}=0$ and $v_{y0}=0$, the isotropic limit with $v_x=v_y=v_F$, this model will reduce to the graphene Hamiltonian. Through the transformation [18,37]

$$\tilde{k}_x=k_x\cos\theta_t+\frac{k_y}{\gamma^2}\sin\theta_t,$$
$$\tilde{k}_y=-k_x\sin\theta_t+\frac{k_y}{\gamma^2}\cos\theta_t, \tag{2}$$

followed by a gauge transformation

$$U=\begin{pmatrix} e^{-i\theta_t/2} & 0 \\ 0 & e^{i\theta_t/2}\end{pmatrix},$$

the tilted Dirac cone Hamiltonian (1) can be rewritten as

$$H(\tilde{k})=\hbar v_x\begin{pmatrix} \eta\tilde{k}_x & \tilde{k}_x-i\tilde{k}_y \\ \tilde{k}_x+i\tilde{k}_y & \eta\tilde{k}_x\end{pmatrix}=\hbar v_x(\eta\tilde{k}_x\sigma_0+\tilde{\boldsymbol{k}}.\boldsymbol{\sigma}). \tag{3}$$

In Eq. (2), the dimensionless parameters η and θ_t determine the tilting characteristic of the system and are defined as

$$\eta=\sqrt{\frac{v_{x0}^2}{v_x^2}+\frac{v_{y0}^2}{v_y^2}},\quad \gamma=\sqrt{v_x/v_y},\quad \cos\theta_t=\frac{v_{x0}}{v_x\eta}. \tag{4}$$

Here, γ is the intrinsic anisotropy, and the tilt parameter is given by $0\leqslant\eta\leqslant 1$. The values of $\eta=0$ and $\gamma=1$ correspond to the graphene case [15,38].

The eigenvalues and eigenstates of the transformed Hamiltonian are given by

$$E_\lambda(\tilde{\boldsymbol{k}})=\hbar v_x\tilde{k}(\lambda+\eta\cos\tilde{\theta}_{\tilde{\boldsymbol{k}}}),\quad |\tilde{\boldsymbol{k}},\pm\rangle=\frac{1}{\sqrt{2}}\begin{pmatrix}1\\ \pm e^{i\tilde{\theta}_{\tilde{\boldsymbol{k}}}}\end{pmatrix}, \tag{5}$$

where $\lambda=\pm$ refers to positive (E_+) and negative (E_-) energy branches, and $\tilde{\theta}_{\tilde{\boldsymbol{k}}}$ is the polar angle of the wave vector, $\tilde{\boldsymbol{k}}$, with respect to the x axis. Note that the angular dependence in Eq. (5) persists even when the anisotropy generated by nonequal v_x, v_y is not present (i.e., when $\gamma=1$). It is the genuine anisotropy due to tilting, as it vanishes when η does. In what follows, to avoid cluttering up with notation, we replace the notation $\tilde{\boldsymbol{k}}$ with $\boldsymbol{k}$, and similarly $\tilde{\theta}_{\tilde{\boldsymbol{k}}}$ with $\theta_{\boldsymbol{k}}$. Note that in the isotropic case, the $\gamma=1$ case considered here, this will imply that the momentum transfers $\boldsymbol{q}$ and $\tilde{\boldsymbol{q}}$ are related by a simple rotation, $\phi=\theta_t+\tilde{\phi}$, where ϕ and $\tilde{\phi}$ are polar angles of the $\boldsymbol{q}$ and $\tilde{\boldsymbol{q}}$.

The polarization function in linear response theory is defined by

$$\chi(\boldsymbol{q},\omega)=\int\frac{dt}{2\pi i}e^{i\omega t}\Theta(t)\langle[\rho_{\boldsymbol{q}}(t),\rho_{-\boldsymbol{q}}(0)]\rangle, \tag{6}$$

the Lehmann representation of which is given by

$$\chi(\boldsymbol{q},\omega)=\frac{g\gamma^2}{A}\lim_{\epsilon\to 0}\sum_{k,\lambda,\lambda'=\pm}\frac{n_{\boldsymbol{k},\lambda}-n_{\boldsymbol{k}',\lambda'}}{\hbar\omega+E_{\boldsymbol{k},\lambda}-E_{\boldsymbol{k}',\lambda'}+i\epsilon}\times f_{\lambda,\lambda'}(\boldsymbol{k},\boldsymbol{k}'). \tag{7}$$

Here, expectation value of density operator between two eigenstates of $|\boldsymbol{k},\lambda\rangle$ and $|\boldsymbol{k}',\lambda'\rangle$ is defined by the form factor $f_{\lambda,\lambda'}(\boldsymbol{k},\boldsymbol{k}')$. The spin degeneracy, which is equal to 2, is included in the constant coefficient g. In this work, as we are concerned with only a single valley, the resulting PH transitions are also considered around one valley. Ignoring the other valley, breaks the inversion symmetry. To restore the inversion symmetry, one has to consider both valleys. The factor of γ^2 comes from the Jacobian of the transformation, Eq. (2). A is the area of the two-dimensional system, and ϵ is defined as an infinitesimal positive constant. The Fermi distribution function is denoted by $n_{\boldsymbol{k},\lambda}$, which at zero temperature reduces to step function. The wave vectors are related by $\boldsymbol{k}' = \boldsymbol{k} + \boldsymbol{q}$, with $\boldsymbol{q}$ being the momentum transfer, the direction of which with respect to x axis is ϕ. In the following, we analytically calculate this polarization function and upgrade a numeric calculation of an existing calculation [34] to an analytical expression, which is benchmarked against the numerical calculation of Ref. [34]. Our result for the imaginary part of the polarization function is identical to that in Ref. [34]. While the authors of this reference use the Kramers-Kronig relation to numerically calculate the real part of the polarization function, we are able to find analytic expressions for the real part, which agrees with the numerical calculations of Ref. [34]. But our result does not agree with a recent calculation [35].

A. Undoped tilted Dirac cone

In the undoped tilted Dirac cone, which corresponds to $\mu = 0$, the states with negative (positive) energy, which are in the lower (upper) part of the cone are always occupied (unoccupied). Hence the Fermi distribution function at zero temperature will be one (zero) for the valence (conduction) band states. Therefore the polarization function (8) reduces to

$$\chi_0(\boldsymbol{q},\omega) = \frac{g\gamma^2}{A}\lim_{\epsilon\to 0}\sum_{k} f_{+,-}(\boldsymbol{k},\boldsymbol{q}) \times\left\{\frac{1}{\hbar\omega + E_{\boldsymbol{k},-} - E_{\boldsymbol{k}+\boldsymbol{q},+} + i\epsilon} - \frac{1}{\hbar\omega + E_{-\boldsymbol{k}-\boldsymbol{q},+} - E_{-\boldsymbol{k},-} + i\epsilon}\right\}. \quad (8)$$

Here the subscript 0 in χ_0 stands for undoped tilted Dirac cone and $f_{-,+}$ is the interband form factor

$$f_{\lambda,\lambda'}(\boldsymbol{k},\boldsymbol{q}) = \tfrac{1}{2}(1 + \lambda\lambda'\cos(\theta_{\boldsymbol{k}} - \theta_{\boldsymbol{k}'})) \quad (9)$$

for $\lambda \neq \lambda'$. Again, to avoid cluttering up with notation, we define an auxiliary frequency

$$\Omega \equiv \hbar\omega - \hbar v_x q\eta\cos\phi, \quad (10)$$

and we work in units where $\hbar = v_x = 1$. Furthermore, according to the fluctuation dissipation theorem for Eq. (8), $\chi_0(\boldsymbol{q},-|\omega|) = \chi_0^*(-\boldsymbol{q},|\omega|)$, which implies $\chi_0(\boldsymbol{q},|\Omega|) = \chi_0^*(-\boldsymbol{q},-|\Omega|)$. Hence we only need to evaluate the integrals for $\Omega > 0$. Doing integration on momentum space and using the Kramers-Kronig dispersion relation (for more details see Appendix B) gives the following result for the imaginary and real parts of the undoped polarization function:

$$\Im\chi_0(q,|\Omega|) = -\frac{gq^2}{16\hbar v_x v_y}\frac{\mathrm{sgn}(\Omega)}{\sqrt{\Omega^2 - q^2}}\Theta(|\Omega| - q), \quad (11)$$

$$\Re\chi_0(q,|\Omega|) = -\frac{gq^2}{16\hbar v_x v_y}\frac{\Theta(q - |\Omega|)}{\sqrt{q^2 - \Omega^2}}. \quad (12)$$

Here, the functional forms of the real and imaginary parts are the same as in the undoped graphene [33]. However, the tilt induced direction dependence is encoded in the definition of $\Omega = \omega - q\eta\cos\phi$. Note that only for undoped graphene the entire tilt dependence enters into the auxiliary frequency Ω. As will be shown in the following, in the case of doped tilted Dirac cone, the tilt dependence will not solely appear through Ω [35], but will in addition, heavily affect the integration limits.

B. Doped tilted Dirac cone

In the case of doped tilted Dirac cone as a result of nonzero chemical potential ($\mu \neq 0$), both processes of intra- and interband transitions contribute to the polarization function [33]. As in the case of graphene, it turns out to be more convenient to subtract the polarization of undoped case from doped one,

$$\Delta\chi(\boldsymbol{q},\omega) = \chi(\boldsymbol{q},\omega) - \chi_0(\boldsymbol{q},\omega),$$
$$\chi(\boldsymbol{q},\omega) = \Delta\chi(\boldsymbol{q},\omega) + \chi_0(\boldsymbol{q},\omega). \quad (13)$$

Then the undoped contribution, χ_0, can be added at the end. As pointed out, the subscript 0 stands for the undoped case. After doing some simplification, $\Delta\chi(\boldsymbol{q},\omega)$ can be rewritten as

$$\Delta\chi(\boldsymbol{q},i\Omega_n) = \frac{g\gamma^2}{A\hbar^2 v_x^2}\sum_{\boldsymbol{k},\lambda}\Theta(\mu - \lambda E_\lambda(\boldsymbol{k}))P(\boldsymbol{k},\boldsymbol{q},i\lambda\Omega_n), \quad (14)$$

where

$$P(\boldsymbol{k},\boldsymbol{q},i\Omega_n) = \frac{(i\Omega_n + k) + k'm}{(i\Omega_n + k)^2 - (k')^2}. \quad (15)$$

Here, $k' = |\boldsymbol{k} + \boldsymbol{q}|$ and $m = \cos(\theta_{\boldsymbol{k}} - \theta_{\boldsymbol{k}'})$. The function $P(\boldsymbol{k},\boldsymbol{q},\pm i\Omega_n)$ is a complex function. The essential point in Eq. (14) is that, in comparison to graphene, the step function not only is a function of k, but also is dependent on the direction of wave vector $\boldsymbol{k}$, which makes the integration more complicated. At the end, we need to perform the Wick rotation, $i\Omega_n \to \Omega + i\epsilon$.

In what follows, in order to calculate the real part of the polarization function for the doped tilted Dirac cone, the infinitesimal imaginary part of $i\epsilon$ can be ignored, and the integration on k becomes a Cauchy principal value. Doing the integration on k, generates a logarithmic function the branch cut of which needs to be carefully handled. This makes the angular integration slightly complicated. Our trick to overcome this difficulty is to represent the logarithm itself as an integral over some auxiliary variable. Then the calculus of residues can be used to perform the angular integration. The integral over the auxiliary variable can be calculated at the end. For details of calculation see Appendix B. The final

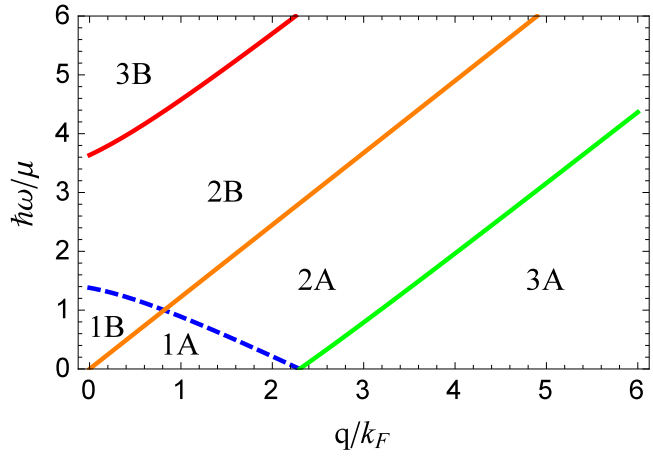

FIG. 1. Different regions in the space of q/k_F and $\hbar\omega/\mu$. Various regions determine the sign structure coming from step functions in the tilted Dirac cone. This figure is produced for the tilt parameter $\eta = 0.45$ and $\phi = \pi/3$, which will be extensively used in this paper. In Ref. [34], a similar figure is produced for $\eta = 0.8$. In the limit $\eta \to 0$, this figure becomes identical to Fig. 6 of Ref. [33]. Part of the dashed border that separates region 1B and 2B is where the plasmon kink develops (see Sec. IV of the main text).

result of integration is summarized as

$$\Re\Delta\chi(\boldsymbol{q},\Omega) = F^1(\boldsymbol{q},\Omega)\Big[G(X^+)\Big|_{x_d^+}^{x_u^+} + \sum G(X^-)\Big|_{x_d^-}^{x_u^-}\Big] + F^0(\boldsymbol{q},\Omega), \tag{16}$$

where

$$F^0(\boldsymbol{q},\Omega) = \frac{g}{16\pi\hbar^2 v_x v_y}\frac{\mu\, q^2}{\sqrt{1-\eta^2}}\frac{A(\boldsymbol{q},\Omega)}{D^2(\boldsymbol{q},\Omega)}, \tag{17}$$

$$F^1(\boldsymbol{q},\Omega) = \frac{g}{16\pi\hbar^2 v_x v_y}\frac{q^2}{\sqrt{|\Omega^2-q^2|}}, \tag{18}$$

$$G(x) = B(\boldsymbol{q},\Omega)x\sqrt{x^2-x'} - \mathrm{sgn}(\Omega-q)\cosh^{-1}\frac{x}{\sqrt{x'}}, \tag{19}$$

and the summation denoted by Σ indicates sum over disconnected pieces. The quantities x' and $X^\pm$ are defined as follows, $x' = (\Omega + q\eta\cos\phi)^2 - (1-\eta^2)(\Omega^2 - q^2)$, and $X^\lambda = 2\tilde{\mu}x + \lambda(\Omega + q\eta\cos\phi)$. The $\tilde{\mu}$ and upper (x_u^λ) and lower (x_d^λ) limits for $\lambda = +(-)$, corresponding to intra(inter)band processes, are limits of integrations which are separately determined for each region in Fig. 1. The details of the derivations of various regions are given in Appendix B. Here, $\mathrm{sgn}(\Omega - q)$ is the sign of $\Omega - q$. The definitions of coefficients $A(\boldsymbol{q},\Omega)$, $B(\boldsymbol{q},\Omega)$, and $D(\boldsymbol{q},\Omega)$ are given in Appendix B. These functions strongly depend on the tilt parameter η, and hence on the direction ϕ of momentum transfer $\boldsymbol{q}$. Therefore the tilt and angular dependence in the doped Dirac cone not only comes through the auxiliary frequency Ω, but it also appears in the coefficients of A, B, and D. The later part is missing in the calculation of Ref. [35].

As a cross-check of our analytic results against the established results on graphene [32,33], if we set the tilt parameter $\eta = 0$, it can be easily seen that the above functions reduce to

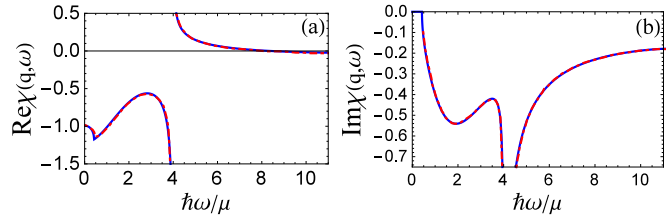

FIG. 2. Comparison of real and imaginary parts of the polarization function for a doped tilted Dirac cone with the result in Ref. [34]. The vertical axis is in units of $\mu/\hbar^2 v_x v_y$ and $v_{x0} = 0.8$ and $v_{y0} = 0$, i.e., $\eta = 0.8$. The momentum q is in the y direction ($\phi = \pi/2$) and equals to 4. The blue (solid) and red (dot-dashed) curves correspond to our calculation and the result in Ref. [34], respectively.

$A(\boldsymbol{q},\Omega) = q^2$, $B(\boldsymbol{q},\Omega) = q^{-2}$. As a result, the real part (16) reduces to the real part of doped graphene polarization function [33].

Now let us look into the simpler calculation, which deals with the imaginary part of polarization function (14) [34]. This can be straightforwardly calculated thanks to a Dirac delta function arising from the small imaginary part $i\epsilon$ in the denominator of Eq. (14). The imaginary part of the polarization function in our notation becomes

$$\Im\Delta\chi(\boldsymbol{q},\Omega) = F_2(\boldsymbol{q},\Omega)\big[G_0^+(x)\big|_{y_d^+}^{y_u^+} + G_0^-(x)\big|_{y_d^-}^{y_u^-}\big], \tag{20}$$

where

$$F_2(\boldsymbol{q},\Omega) = \frac{g}{32\pi\hbar^2 v_x v_y}\frac{q^2}{\sqrt{|\Omega^2-q^2|}},$$
$$G_0^+(x) = x\sqrt{x^2-1} - \cosh^{-1}x, \tag{21}$$
$$G_0^-(x) = x\sqrt{1-x^2} + \sin^{-1}x.$$

Here the upper (y_u^λ) and lower (y_d^λ) limits are defined by the roots of Fermi distribution (step function at zero temperature). Their explicit expressions are given in Appendix C.

Again it can be seen (see Appendix C) that in the case of $\eta = 0$, the imaginary part as well, will be reduced to the case of graphene. Finally, as the last step, we should add the undoped polarization function to the $\Delta\chi(\boldsymbol{q},\Omega)$ to derive the doped polarization function. Let us emphasize again that the relation between the real momentum coordinate $\boldsymbol{q}$ and the auxiliary momentum $\tilde{\boldsymbol{q}}$ is given by the linear transformation (2). In the special case of $\gamma = 1$, it becomes a simple rotation $\phi \to \phi - \theta_t$. If we use our freedom to choose the k_x axis to lie along the k_x axis, then θ_t will be eliminated from the density-density response.

C. Benchmark against existing results

Nishine and coworkers have already obtained the analytical formula for the imaginary part [34]. For the real part, they numerically perform the Kramers-Kronig transformation. Therefore they have numerical results for the $\mathrm{Re}\chi(\boldsymbol{q},\omega)$. Let us ensure that our analytic results agree well with their results. In the following, we reproduce some of the plots related to their work. In Fig. 2(a), we compare our analytic Eq. (16) for the real part of polarization (solid blue curve) with the numerical result of Nishine and coworkers (red dot-dashed). As can

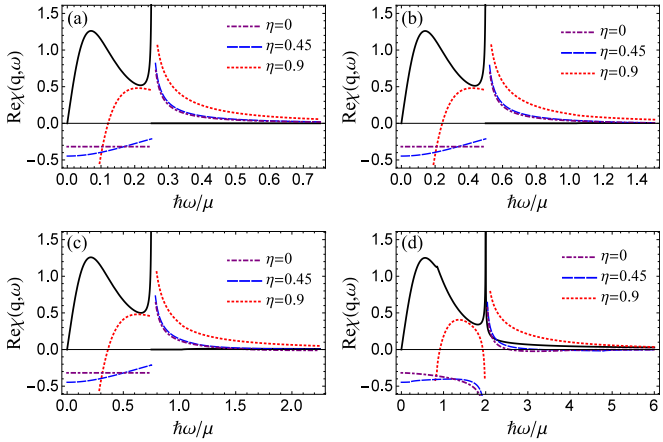

FIG. 3. Real part of the polarization function for a doped tilted Dirac cone, for different values of η as indicated in the legend. The direction of $\boldsymbol{q}$ is fixed by $\phi = \pi/2$. The vertical axis is in the unit $\mu/\hbar^2 v_x v_y$ and the horizontal axis is a dimensionless quantity $\hbar\omega/\mu$. The magnitude of q/k_F in the various panels is 0.25 in (a), 0.5 in (b), 0.75 in (c), and 2.0 in (d). The solid line is the imaginary part of χ for $\eta = 0.9$. For explanation see the text.

be seen, the agreement is perfect. Panel (b) of this figure compares the imaginary parts adopted from their curves with those produced by our Eq. (20). The comparisons are made for $\eta = 0.8$ used in Ref. [34]. Also in both cases, the vertical axis is in units of $\mu/\hbar^2 v_x v_y$. Again, as can be seen, the agreement is perfect. Our analytical formula for the real part will enable us to analytically explore the plasmons and screening in tilted Dirac cone. In the following section, we start with a qualitative discussion of plasmons in presence of tilt.

III. PLASMONS: ROLE OF TILT PARAMETER η

One of the significant collective excitations of the electronic systems in the long-wavelength limit is the plasmon, which augments the single-particle picture of an electron gas at the lattice scale with a self-organized collective oscillation of appropriate electric fields and charge densities [39,40]. In a two-dimensional electron gas, whether Dirac [7] or non-Dirac, the plasmon dispersion relation at the long-wavelength limit is given by $\omega_{\rm pl} \propto \sqrt{q}$. Indeed, this follows from a general hydrodynamic consideration [41]. In the linear response formulation, plasmons are zeros of the dielectric function. Within the RPA approximation, the dielectric function will be given by

$$\varepsilon(\boldsymbol{q}, \omega) = 1 - V_q \chi(\boldsymbol{q}, \Omega), \tag{22}$$

where, in a single layer of the two-dimensional system, the Coulomb interaction is given by $V_q = 2\pi e^2/q$, and χ is the bare electron-hole bubble. Since V_q is a positive quantity, a necessary condition to obtain a plasmon branch of excitations is to require that the real part of density response function is positive.

In Fig. 3, we have plotted the real part of the polarization function χ (in the unit $\mu/\hbar^2 v_x v_y$) for different values of η. The dot-dashed, dashed, and dotted plots correspond to $\eta = 0$, 0.45, and 0.9, respectively, as indicated in the legend. The four panels (a), (b), (c), and (d) correspond to

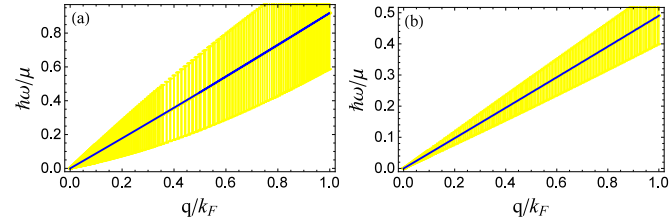

FIG. 4. The overdamped plasmon mode arising from tilt for the direction $\phi = \pi/2$. Left (right) panel corresponds to tilt parameter $\eta = 0.75$ ($\eta = 0.9$). The shaded region represents damping. The amount of damping in the right panel is decreased by a factor of 10 to fit in the panel.

$q = |\boldsymbol{q}| = 0.25$, 0.5, 0.75, and 2.0, respectively. Since the polarization function is strongly anisotropic, in this figure we have fixed the direction ϕ of $\boldsymbol{q}$ to be at $\phi = \pi/2$. The solid line is the imaginary part plot of χ for $\eta = 0.9$ only. The above collective mode equation in units of $\hbar = v_x = 1$ can be written in the dimensionless form, $\mathrm{Re}\chi = \bar{q} v_y/(\alpha c)$, where $\alpha = 1/137$ is the fine structure constant, c is the velocity of light, dimensionless in their natural units. For example, q is meant in units of k_F. Quite generally, the imaginary part of χ abruptly changes at $\omega_+ = q(1 + \eta\cos\phi)$, which marks the upper border of intraband PH excitations in the tilted Dirac cone [34]. For $\phi = \pi/2$, this reduces to $\omega_+ = q$. This is why in both the real part and the imaginary part (solid line) there is a discontinuity at this energy scale, which for $\phi = \pi/2$, coincides with q itself. The plasmon mode is obtained by intersecting a constant horizontal line (given by the above dimensionless equation) with the real part of χ. Let us first focus on $\omega > \omega_+$ region (1B in Fig. 1), where the $\mathrm{Im}\chi$ is identically zero. As can be seen in all figures, by increasing the tilt parameter η, the real part of χ is lifted to larger values. This, in turn, will shift the plasmon modes to higher energies. Therefore the generic effect of the increase in the tilt is to shift the plasmons to higher energies. The $\eta = 0$ case would correspond to the graphenelike situation. This is the standard plasmon branch. This branch will continue to the 2B region of Fig. 1, but will acquire small damping as there is a small density of interband PH excitations in 2B.

Now let us look into $\omega < \omega_+$ (corresponding to region 1A in Fig. 1), where the imaginary part is nonzero and non-negligible. It is curious to note that for large values of η (the red dotted line in all panels), the real part of χ for $\omega < \omega_+$ becomes positive. This implies a lower-energy plasmon branch. However, since in the natural units, the magnitude of the imaginary part—which quantifies the density of free intraband PH states (black, solid line) available for Landau damping—is $\mathcal{O}(1)$, such a tilt induced extra plasmon branch will be overdamped. The dispersion of overdamped plasmon branch is shown in Fig. 4. The shaded region indicates the damping; larger width means larger damping [42]. As can be seen, the mode disperses linearly, but it is heavily damped. In the right panel corresponding to $\eta = 0.9$ the damping is so large that, in order to fit in the panel, we have reduced the shaded region indicating the damping by a factor of 10. Note that for $\eta = 0$ situation pertinent to graphene, the real part for $\omega < \omega_+$ can never be positive, and hence no extra plasmon solution is conceivable.

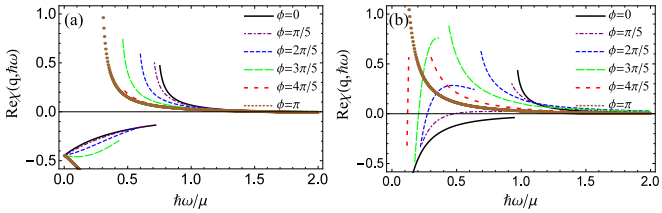

FIG. 5. Real part of χ in units of $\mu/\hbar^2 v_x v_y$ as a function of dimensionless $\hbar\omega/\mu$ for fixed $q/k_F = 0.5$ and various values of angle ϕ indicated in the legend. The left (right) panel corresponds to $\eta = 0.45$ ($\eta = 0.9$).

The above discussion in Fig. 3 was for a fixed $\phi = \pi/2$ orientation of $\boldsymbol{q}$. Let us now explore the direction dependence. Since the density response is strongly anisotropic, in Fig. 5, we have shown the angular dependence of Reχ. Solid (black), dot-dashed (purple), dashed (blue), long-dashed (green), sparse-dashed (red), and dotted (brown) correspond to $\phi = n\pi/5$ for $n = 0,\ 1,\ 2,\ 3,\ 4,$ and 5, respectively. The left (right) panel corresponds to the tilt parameter $\eta = 0.45$ ($\eta = 0.9$). The first observation concerns the $\omega > \omega_+$ (1B in Fig. 1) region. As can be seen by increasing ϕ from 0 to π in both panels, the Reχ curves are pushed to the left as ω_+ itself depends on the angle ϕ. Therefore the corresponding plasmons will have smaller energies. The second observation, which is the essential difference between the left ($\eta = 0.45$) and right ($\eta = 0.9$) panel, is concerned with the $\omega < \omega_+$ (1A in Fig. 1) region. As can be seen for $\eta = 0.9$ in the right panel, for all angles, except $\phi = 0$, the Reχ develops a positive branch which gives rise to overdamped plasmons in $\omega < \omega_+$ (1A in Fig. 1) region. This indicates that the additional overdamped plasmon branch is solely due to (large enough) the tilt of the Dirac cone.

Quite generally, the anisotropy can come from two sources: (i) the intrinsic anisotropy due to $v_x \neq v_y$, or equivalently $\gamma \neq 1$; and (ii) the tilt also acts as a source of anisotropy which is manifested in Fig. 5 as a strong angular dependence of the Reχ-vs-ω curves. To investigate this further, in Fig. 6, we have plotted the constant energy contours of the plasmon dispersion

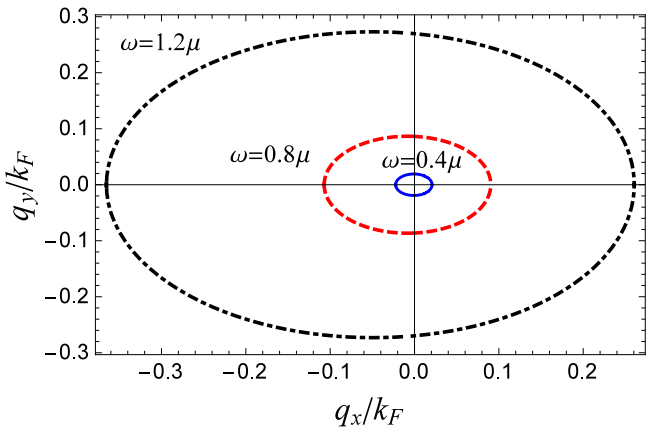

FIG. 6. Constant energy cuts of the plasmon dispersion for a moderate tilt parameter $\eta = 0.45$. Curves are generated for $v_x = v_y = c/1000$.

for a fixed tilt parameter $\eta = 0.45$, for three representative energies as indicated in the figure. The contours clearly indicate a tilt pattern. Moreover, it is manifestly symmetric with respect to $\phi \to -\phi$, which is expected from the Hamiltonian, as we have assumed the tilt is along k_x axis. The plasmonic energy contours in Fig. 6 reflect the sole effect of tilt parameter, as we have generated this figure for $v_x = v_y$. When the tilt parameter is set to zero, the above ellipses become concentric, and the aspect ratio becomes 1, meaning that the ellipses become circles. The above curve is not inversion symmetric with respect to the origin of the tilt axis (assumed to be along x axis). This is because we have considered only one tilted Dirac cone. A second cone with opposite tilt will restore the inversion symmetry.

IV. TILT-INDUCED KINK IN THE PLASMON DISPERSION

In the case of graphene where the tilt parameter η is zero, the region 1B of Fig. 1 reduces to a triangular region which is void of free PH pairs, and separates the intraband (lower side) continuum of PH excitations from the interband (upper side) continuum. The plasmons in region 1B are well defined. The plasmon branch, however, continues to disperse inside the region 2B of Fig. 1, which contains very small amount of DOS of interband PH excitations. Therefore the plasmon branch continuously enters the interband PHC with a negligible damping [32]. By turning on the tilt parameter, η, the density of interband PH states in region 1B will not change significantly. Therefore the plasmon branch will continue to the region 2B with negligible damping. But as we will see in this section, the tilt parameter will induce a kink at the border separating regions 1B and 2B (dashed line in Fig. 1).

Let us start by monitoring the evolution of plasmon branch as the tilt parameter grows from zero. In Fig. 7, we have plotted the dispersion of plasmons in the plane of $\hbar\omega/\mu$ and q/k_F. Panels (a)–(f) correspond to angles $\phi = n\pi/5$ with $n = 0, \ldots, 5$. Various curves as indicated in the legend correspond to tilt parameters $\eta = 0, 0.3, 0.45, 0.6, 0.9$. The first point to notice is the following: a common aspect of all panels (all directions) in Fig. 7 is that in the long wavelength limit for a fixed small q, the energy of the plasmon resonance increases by increasing the tilt parameter η. This is true for all angles in panels (a) to (f). Such ordering in the energy of plasmon resonances in terms of η does not hold for larger q values, anymore. The second point to notice is that for $\phi = \pi$ in panel (f), the plasmon dispersion is less sensitive to the tilt parameter η. Note that the asymmetry between the $\phi = 0$ and π in panels (a) and (f) is related to considering only one valley. Considering both valleys will restore the broken inversion symmetry. This is because in the tilted Dirac material, the two tilted Dirac cones have opposite tilt direction. Therefore keeping only one Dirac cone amounts to manually breaking the inversion symmetry. Therefore, taking the second valley into account, will restor only the inversion symmetry, but still the full rotational symmetry will be absent.

The third and most remarkable point to notice is the appearance of a kink in the plasmon dispersion. This is more manifest in panels (c) and (d) corresponding to $\phi = 2\pi/5$ and $\phi = 3\pi/5$, respectively. Indeed, the most manifest form of kink appears for $\phi = \pi/2$. The kink is present for any nonzero

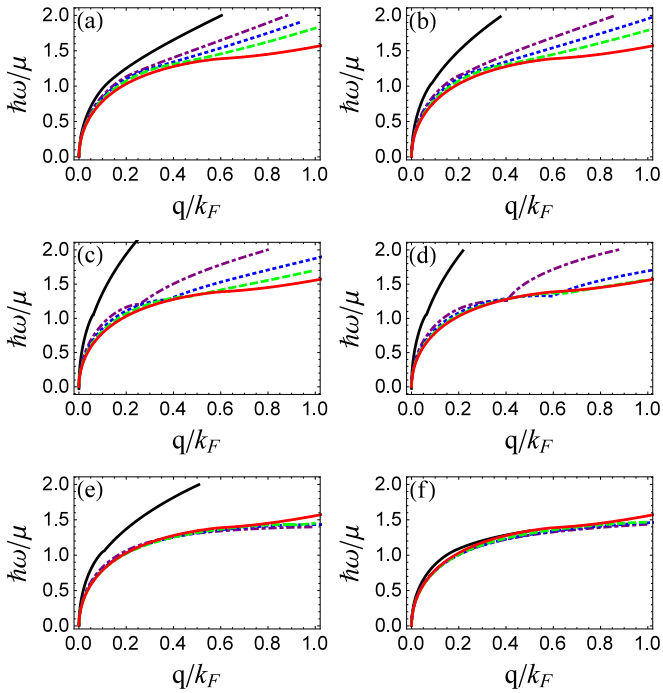

FIG. 7. Dependence of plasmon dispersion on the tilt parameter η and angle ϕ. The horizontal axis is q/k_F and the vertical axis is $\hbar\omega/\mu$. The tilt parameters $\eta = 0, 0.3, 0.45, 0.6, 0.9$ are encoded as solid (red), dashed (green), dotted (blue), dot-dashed (purple), and the leftmost solid (black) curves, respectively. (a)–(f) correspond to directions $\phi = \pi n/5$, with $n = 0, \ldots, 5$.

tilt parameter η. Therefore *the above anisotropic kink is a direct manifestation of the tilt*. This fact can be used to directly map the tilt parameter from the angle-resolved electron energy loss spectroscopy (EELS). The kink is very anisotropic. To bring this out, in Fig. 8, for a fixed moderate value of $\eta = 0.45$ [18], we have plotted the plasmon dispersion for various angles. As can be seen, the position of kink is very sensitive to the direction ϕ of the momentum $\boldsymbol{q}$ of the plasmon excitations.

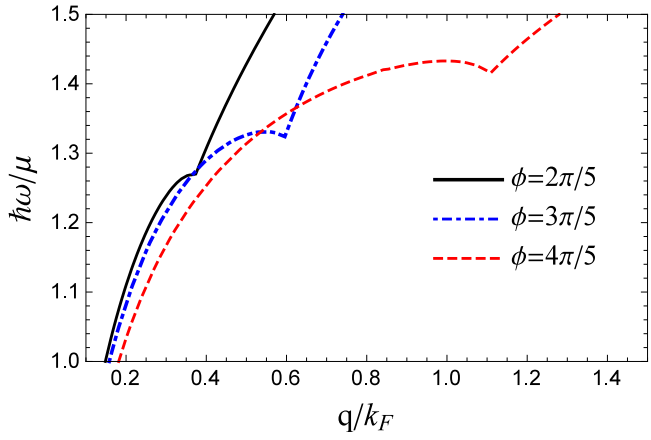

FIG. 8. Angular dependence of the plasmonic kink. The figure is produced for the moderate tilt parameter $\eta = 0.45$, pertinent to realistic materials [18].

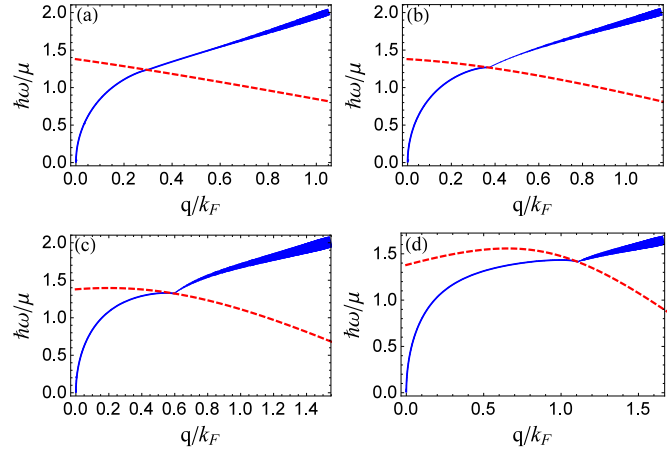

FIG. 9. The position of the kink for the tilt parameter $\eta = 0.45$. The solid (blue) line is the plasmon dispersion, and the dashed (red) curve is the $\omega_A(q)$ given by Eq. (23). (a)–(d) correspond to $\phi = n\pi/5$ with $n = 1, 2, 3, 4$, respectively. Note that the width of the plasmon dispersion in region 2B is exaggerated by a factor of 50 to emphasize very small damping.

A. Origin of the kink and direct experimental measurement of the tilt parameter

To investigate the origin of kink, in Fig. 9 we have plotted the plasmon dispersion (the solid, blue, curve) for the tilt parameter $\eta = 0.45$ and different momentum direction as $\phi = n\pi/5$ with $n = 1, 2, 3, 4$ for panels (a)–(d). The thickness is associated with the damping of plasmons. To be clear, we have exaggerated the thickness by a factor of 50. This clearly indicates that the emergence of kink goes hand in hand with the onset of damping. Therefore the kink appears at the border separating regions 1B and 2B of Fig. 1. To verify this, we have plotted the border formula by dashed (red) line. As is expected, the kink begins exactly when the plasmon branch crosses this border.

The formula for the dashed border, which now, in hindsight, can be dubbed *kink energy scale*, is given by [34]

$$\omega_{\text{kink}} = q\eta\cos\phi + \frac{2}{1-\eta^2} - \sqrt{q^2 + \frac{4q\eta\cos\phi}{1-\eta^2} + \left(\frac{2\eta}{1-\eta^2}\right)^2}, \qquad (23)$$

where ω_{kink} and q are dimensionless energy and momentum scales in the units $\mu/\hbar$ and k_F, respectively. The above energy scale is denoted by ω_A in Ref. [34], and defines the upper border of the region denoted as 1B in Fig. 1. This region is defined in

$$q(1+\eta\cos\phi) < \omega < \omega_{\text{kink}}, \quad q < 1. \qquad (24)$$

It can be easily checked that, for $\eta = 0$, this region reduces to the triangular region that separates the inter- and intraband portion of PHC in doped graphene [32,33]. When the borders coincide with that of the triangular 1B region of the $\eta = 0$ situation, the parts of the plasmon branch in 1B and 2B regions connect to each other without any kink [32]. However, the tilt pushes the upper boundary of the triangle down, and

distorts it to the dashed curve in Fig. 1, whereby a kink in the dispersion of plasmon branch is generated.

The above kink in plasmon dispersion allows for a direct measurement of the tilt parameter. As pointed out, beyond the kink that the plasmon dispersion enters the continuum of interband PH excitations, the imaginary part of the polarization function χ is negligibly small (the width of the plasmon in Fig. 9 is exaggerated by a factor of 50 to emphasize the connection between damping and kink). Therefore the plasmon excitations with wave vectors larger than the kink scale are expected to live long enough to allow for experimental detection.

Suppose that for a fixed direction $\phi_{\rm exp}$, the kink is experimentally determined to occur at $(q_{\rm exp}, \omega_{\rm exp})$. Then the tilt parameter η satisfies the following equation:

$$\omega_{\rm exp} = \omega_{\rm kink}(q_{\rm exp}, \phi_{\rm exp}, \eta), \tag{25}$$

where the $\omega_{\rm kink}$ function in the right-hand side is given by Eq. (23). All quantities with the suffix "exp" can be directly measured in the experiment. Therefore the only unknown in Eq. (25) is the tilt parameter η. Therefore this equation enables a *direct* experimental measurement of the tilt parameter, η. A measurement of the tilt by optical experiments has also been suggested [43]. It would be interesting to compare the results for a tilt parameter from optical measurements and our present suggestion based on an EELS measurement [36].

V. ASYMPTOTIC FORMULA

The hydrodynamic limit in electron liquids is quite generally given by small temporal and spatial variations, $\omega \to 0$ and $q \to 0$. The ratio of ω and q, however, can be finite. We are working in units where the velocities $v_x = v_y = 1$ and $\hbar = 1$. Hence the ratio ω/q is dimensionless. The tilt parameter, η, being dimensionless, enters the game through a combination $\omega\eta/q$. Let us see this by asymptotically expanding our analytic formula for the ${\rm Re}\chi$.

A. Tilt-dependence of plasmons

In order to investigate the plasmon dispersion in tilted Dirac cone, we first find the long wavelength limit of polarization function. As pointed out, the tilt parameter appears as the $\omega\eta/q$ combination. In the long wavelength limit ($q \to 0$) our formula gives

$$\begin{aligned}&{\rm Re}\chi(q \to 0, \omega)\\ &\approx \begin{cases} \frac{D_0 q^2}{4\pi\omega^2}\left(1 - \frac{2\omega\eta}{q}\right), & \eta \ll q, \quad \frac{\omega\eta}{q} \ll 1 \\ \frac{D_0 q^2}{4\pi\omega^2\eta^2}[\cos 2\phi + H(\eta)], & \eta \gg q, \quad \frac{\omega\eta}{q} \gg 1 \end{cases},\end{aligned} \tag{26}$$

with

$$H(\eta) = \frac{\eta^2 + (\eta^2 - 2)\cos 2\phi}{\sqrt{1-\eta^2}}, \quad D_0 = \frac{g\mu}{4\pi\hbar^2 v_x v_y}, \tag{27}$$

where we have restored the constants $\hbar, v_x, v_y$. The $\eta \ll q$ piece is continuously connected to $\eta \to 0$. Indeed, setting $\eta = 0$ in the first piece of the above function, we obtain the correct expression for graphene [33]. Therefore one recovers the standard plasmon dispersion of graphene given by [32,33]

$$\hbar\omega_{\rm pl} = \hbar\omega_0\sqrt{q}, \tag{28}$$

where $\omega_0 = \sqrt{g\mu e^2/(8\pi v_x v_y)}$ is set by doping, μ, and Coulomb interaction e^2. As pointed out, the $\sqrt{q}$ plasmonic dispersion is a generic characteristic of 2D systems and can be obtained from hydrodynamic treatment [41].

Now let us look at the other limit where q is still very small, but η is finite such that the combination $\omega\eta/q$ is very large. In this regime, the second piece of Eq. (26) determines the behavior of plasmons. Therefore the plasmon dispersion is given by

$$\hbar\omega_{\rm pl} = \hbar\omega_\eta\sqrt{q}, \quad \omega_\eta = \omega_0\frac{\sqrt{\cos 2\phi + H(\eta)}}{\eta}. \tag{29}$$

Note that due to the piecewise nature of Eq. (26), the $\eta = 0$ in Eq. (29) does not reduce it to Eq. (28). The $\eta = 0$ limit is consistent with the first piece of Eq. (26). As can be seen in the case of tilted Dirac cone dispersion, in addition to dependence on the tilt parameter, η, there is a substantial dependence on the angle ϕ of the wave vector $\boldsymbol{q}$. It is not surprising that the presence of tilt does not change the generic $\sqrt{q}$ dependence of the plasmon oscillations in a monolayer, as it follows from quite general hydrodynamic arguments [41].

B. Tilt enhances the static screening

Now let us look at the opposite limit where ω is set to zero. The static polarization contains information about the screening of external charges in the ground state. In the limit of low frequency, setting $\omega = 0$ implies $\Omega = -q\eta\cos\phi$. Notice that depending on the orientation ϕ of the wave vector $\boldsymbol{q}$ with respect to x axis, the auxiliary frequency Ω can be either a positive or a negative quantity. From the general expression in Eq. (16), for negative Ω (corresponding to $\cos\phi > 0$), we can find the following representation of polarization for any q and $0 < \phi < \pi$:

$$\begin{aligned}{\rm Re}\chi(0, \boldsymbol{q}) = &-\frac{g\mu}{2\pi\hbar v_x v_y\sqrt{(1-\eta^2)^3}}\\ &\times\left[1 + \Theta(\check{q} - 2\mu) f\left(\frac{\check{q}}{2\mu}\right)\right],\end{aligned} \tag{30}$$

where we have restored the constants $\hbar, v_x, v_y$. The $\check{q}$ is defined as $\check{q} = q\sqrt{(1-\eta^2)(1-\eta^2\cos^2\phi)}$ and

$$\begin{aligned}f\left(\frac{\check{q}}{2\mu}\right) = &-\frac{q^2}{2\check{q}^2}\sqrt{1 - \left(\frac{2\mu}{\check{q}}\right)^2}(1-\eta^2)(1-\eta^2\cos 2\phi)\\ &+ \frac{q^2}{4\check{q}\mu}\cos^{-1}\left(\frac{2\mu}{\check{q}}\right).\end{aligned} \tag{31}$$

Again, the first point to note is that for $\eta \to 0$, the above expression reduces to the corresponding expression of graphene [32,33,44]. The second point to notice is that, the screening is controlled by doping μ, and will be ineffective when $\mu = 0$, as there will be no single-particle DOS at the Fermi level to take care of screening. This argument holds for any tilt parameter, in agreement with Eq. (30). The third point to notice is the strong direction dependence of screening.

To manifestly see the role of tilt in screening, let us consider a very special regime corresponding to $\check{q} < 2\mu$. In this situation, the second term in Eq. (30) goes away, and the above

relation will become q-independent. Then it can be easily seen that the screening is controlled by $\mu(1-\eta^2)^{-3/2}$. In the $\eta \to 0$ limit, it reduces to the standard formula of graphene, while for $\eta \to 1$, the above quantity diverges. Therefore, as far as static screening is concerned, the role of very large $\eta \lesssim 1$ is to effectively enhance μ according to the above formula. Therefore, for a fixed doping level, the larger tilt η is expected to give rise to better screening.

VI. SUMMARY AND CONCLUSION

In this paper, we obtained an analytic representation of the full polarization function for a single tilted Dirac cone with arbitrary tilt parameter, $0 \leqslant \eta < 1$, in two space dimensions and arbitrary doping. Our formula agrees with the numerical evaluation of the real part of polarization in Ref. [34] that numerically implements Kramers-Kronig relation. Our result does not agree with Ref. [35], and the reason is that the tilt parameter affects the results both through the auxiliary frequency, Eq. (10), *and through the limits of integration*.

Our analytic formula enables us to find—in addition to a trivial tilt-induced anisotropy—two interesting plasmonic effects. First of all, for strong enough tilt, a new branch of overdamped plasmon appears, which overlaps with a large DOS of intraband PH excitations. When the tilt parameter is zero or even small, there is no chance for such an overdamped plasmonic mode that disperses linearly. Since this overdamped mode energetically overlaps with intraband PHC, it is expected to affect the single-particle properties. Secondly, the upper boundary of the region 1B in Fig. 1 is strongly modified by the tilt. This modification gives rise to a kink in the plasmonic dispersion, the position of which is right at the dashed border in Fig. 1 that separate 1B and 2B regions. In region 2B, the mode acquires a negligible damping which is due to its overlap with interband PH excitations. The small damping allows the branch in region 2B to live long enough to allow for an experimental detection of the kink in the plasmonic dispersion. This has been summarized in Fig. 10, where for the direction $\phi = \pi/2$ with respect to the tilt direction we have plotted the plasmon dispersion along with the imaginary part of the loss function.

The analytic formula for the kink energy scale in Eq. (25) can be used for a direct experimental measurement of the kink parameter by measuring the wave vector $\boldsymbol{q}$ and energy ω at which the kink is taking place. The static limit of our analytic formula shows that for a fixed chemical potential μ, bringing the tilt very close to 1 will substantially enhance the screening. In these appendices, we provide the detailed derivation of the analytic form of the polarization function for a tilted two-dimensional Dirac cone.

APPENDIX A: UNDOPED CASE

The undoped polarization function (8) consists of two terms. The second term is the same as the first term if we replace $\Omega \to -\Omega$. The form factor is defied as

$$f_{\lambda,\lambda'}(\boldsymbol{k},\boldsymbol{q}) = f_{\lambda,\lambda'}(\boldsymbol{k},\boldsymbol{k}') = \langle \boldsymbol{k},\lambda||\boldsymbol{k}',\lambda'\rangle = \tfrac{1}{2}(1+\lambda\lambda'\cos(\theta_{\boldsymbol{k}}-\theta_{\boldsymbol{k}'})). \tag{A1}$$

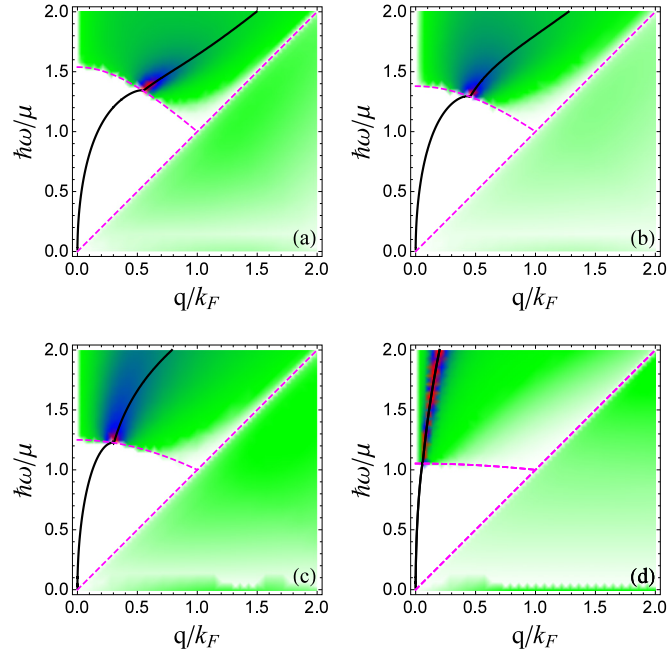

FIG. 10. Imaginary part of the loss function $\mathrm{Im}|1/\varepsilon(\boldsymbol{q},\omega)|$ and the dispersion of the plasmons for different tilt parameters and fixed momentum direction $\phi = \pi/2$. The solid line is the plasmon dispersion, and the dashed curve denotes the borders of the PHC. The lower bound of the interband PHC is the ω_{kink}, which is given by Eq. (23). The tilt parameter in (a)–(d) is $\eta = 0.3, 0.45, 0.6, 0.9$, respectively.

For simplicity of calculation, we change the integration variable $\theta - \phi \to \theta$ (note that for the polar angle $\theta_{\boldsymbol{k}}$ of the integration variable $\boldsymbol{k}$ we simply use θ, and the polar angle of $\boldsymbol{q}$ is ϕ) and find

$$\cos(\theta_{\boldsymbol{k}}-\theta_{\boldsymbol{k}'}) = \frac{k+q\cos\theta}{|\boldsymbol{k}+\boldsymbol{q}|}, \qquad |\boldsymbol{k}+\boldsymbol{q}| = \sqrt{k^2+q^2+2kq\cos\theta}. \tag{A2}$$

Let us start with the imaginary part, which is easier,

$$\Im\chi_u(\boldsymbol{q},\Omega) = -\frac{g\pi\gamma^2}{A\hbar v_x^2}\lim_{\epsilon\to 0}\sum_{k} f^{ij}_{-,+}(\boldsymbol{k},\boldsymbol{q}) \times\{\delta(\Omega-k-|\boldsymbol{k}+\boldsymbol{q}|) - \delta(\Omega+k+|\boldsymbol{k}+\boldsymbol{q}|)\}. \tag{A3}$$

Here, we replaced $v_x k \equiv k$, $v_x q \equiv q$, $v_{x0} = \eta v_x \cos\theta_t$, $v_{y0} = \eta v_y \sin\theta_t$, and $\Omega \equiv \omega - q\eta\cos\phi$. Furthermore, in Eq. (A3), the first (second) term is nonzero whenever $\Omega > 0$ ($\Omega < 0$). By the fluctuation dissipation theory, we find $\Im\chi_0(q,|\Omega|) = -\Im\chi_0(q,-|\Omega|)$ or $\Im\chi_0(\boldsymbol{q},|\omega|) = -\Im\chi_0(-\boldsymbol{q},-|\omega|)$. So we need to do the integration only for one sign of Ω. In the following, we perform the momentum space integration for only the first term in Eq. (A3), which gives

$$\Im\chi_0(q,|\Omega|) = -\frac{gq^2}{16\hbar v_x v_y}\frac{\mathrm{sgn}(\Omega)}{\sqrt{\Omega^2-q^2}}\Theta(|\Omega|-q). \tag{A4}$$

Here we used

$$\delta(\Omega - k - |\boldsymbol{k}+\boldsymbol{q}|) = \frac{|\boldsymbol{k}+\boldsymbol{q}|}{kq}\frac{\delta(\theta-\theta_0)}{|\sin\theta_0|},$$
$$\cos\theta_0 = \frac{\Omega^2 - 2\Omega k - q^2}{2kq}, \tag{A5}$$

which given the fact that $-1 \leqslant \cos\theta_0 \leqslant 1$, implies $\Omega > q$ and $\Omega - q \leqslant 2k \leqslant \Omega + q$. Using Kramers-Kronig dispersion relation, the real part will be given by principle integration on domain ω' as

$$\Re\chi_0(q,\omega) = \frac{p}{\pi}\int_{-\infty}^{+\infty}\frac{\Im\chi_0(\boldsymbol{q},\omega')}{\omega'-\omega}d\omega'$$
$$= \frac{p}{\pi}\int_{-\infty}^{+\infty}\frac{\Im\chi_0(q,\Omega')}{\Omega'-\Omega}d\Omega', \tag{A6}$$

By substitution of $\Omega'^2 - q^2 = t^2$, and doing integration on $0 \leqslant t \leqslant \epsilon_D$ (ϵ_D is energy cutoff which goes away by dimensional regularization [45]), we find

$$\Re\chi_0(q,|\Omega|) = -\frac{gq^2}{16\hbar v_x v_y}\frac{\Theta(q-|\Omega|)}{\sqrt{q^2-\Omega^2}}. \tag{A7}$$

The above expressions are identical to that of up-right (non-tilted) Dirac cone, except that $\omega \to \Omega = \omega - q\eta\cos\phi$. This is only true for the undoped tilted Dirac cone. In the doped cases, as we will see, the tilt will heavily affect the limits of integration. Ignoring this point gives rise to an incorrect result [35].

APPENDIX B: DOPED CASE

The polarization function of tilted Dirac cone in the doped case has a more complicated structure due to the combination of two effects: (i) the angular dependence of the single-particle dispersion and (ii) the nonzero chemical potential. In order to find the real and imaginary parts of polarization, we subtract the polarization function of the undoped system, and then finally after doing the integration on $\boldsymbol{k}$ space, we add it back. If we subtract Eq. (8) and toggle the integration variables in terms involving $\Theta(\mu - E_{\boldsymbol{k}',+})$ as $\boldsymbol{k} \leftrightarrow -\boldsymbol{k}'$ and $\theta_{\boldsymbol{k}} \leftrightarrow \theta_{\boldsymbol{k}'} + \pi$ ($\boldsymbol{k}' = \boldsymbol{k} + \boldsymbol{q}$), we find

$$\Delta\chi(\boldsymbol{q},\Omega) = \frac{g\gamma^2}{2A\hbar^2 v_x^2}\sum_{\boldsymbol{k}}\Bigg\{\Theta(\mu - k - k\eta\cos\theta_{\boldsymbol{k}})\left(\frac{1+\cos(\theta_{\boldsymbol{k}}-\theta_{\boldsymbol{k}'})}{\Omega+k-k'+i\epsilon} + \frac{1-\cos(\theta_{\boldsymbol{k}}-\theta_{\boldsymbol{k}'})}{\Omega+k+k'+i\epsilon}\right)$$
$$- \Theta(\mu - k + k\eta\cos\theta_{\boldsymbol{k}})\left(\frac{1+\cos(\theta_{\boldsymbol{k}}-\theta_{\boldsymbol{k}'})}{\Omega-k+k'+i\epsilon} + \frac{1-\cos(\theta_{\boldsymbol{k}}-\theta_{\boldsymbol{k}'})}{\Omega-k-k'+i\epsilon}\right)\Bigg\}. \tag{B1}$$

It consists of two parts that can be transformed to each other by $\Omega \to -\Omega$ and $\eta \to -\eta$. The important point in doing the rest of the calculation is that in Eq. (14) the step function depends on the direction of wave vector $\boldsymbol{k}$ with respect to x axis. In what follows, we change the integration variable $\theta_{\boldsymbol{k}}$ as $\theta + \phi \to \theta$, which causes the denominators to be independent of the direction ϕ of $\boldsymbol{q}$ and we will have $k' = \sqrt{k^2+q^2+2kq\cos\theta}$. However, the step functions corresponding to Fermi occupation numbers will depend on the direction of both $\boldsymbol{q}$ and $\boldsymbol{k}$. This makes the angular integration slightly more complicated than the cases without angular-dependent energy spectrum—like graphene. It turns out to be more convenient if we first perform the k integration and finally do the angular integration on θ by using the calculus of residues [46].

1. Real part

The real part of polarization $\Delta\chi$ can be represented as a Cauchy principal value. This amounts to setting the imaginary part in the denominator of Eq. (14) equal to zero,

$$\Re\Delta\chi(\boldsymbol{q},\Omega) = \frac{g\gamma^2}{4\pi^2\hbar^2 v_x^2}\int d\boldsymbol{k}\Bigg\{\Theta(\mu - k - k\eta\cos(\theta+\phi))\frac{(\Omega+k)+k'm}{(\Omega+k)^2-(k')^2}$$
$$+ \Theta(\mu - k + k\eta\cos(\theta+\phi))\frac{(-\Omega+k)+k'm}{(-\Omega+k)^2-(k')^2}\Bigg\},$$

where m is the new representation of $\cos(\theta_k - \theta_{k'})$ after above changing variable and represents as $(k + q\cos\theta)/k'$. Now we do integration on k, where the step function determines the upper limit k as

$$\Re\Delta\chi(\boldsymbol{q},\Omega) = \frac{g\gamma^2}{4\pi^2\hbar^2 v_x^2}\int d\theta\int_0^{\mu/(1+\eta\cos(\theta+\phi))}kdk\frac{(\Omega+k)+k'm}{(\Omega+k)^2-(k')^2} + \int d\theta\int_0^{\mu/(1-\eta\cos(\theta+\phi))}kdk\frac{(-\Omega+k)+k'm}{(-\Omega+k)^2-(k')^2}.$$

In the following, we separate the first ($+\Omega$) and second ($-\Omega$) terms of the above relation. The integration on k gives a combination of simple fractions and logarithmic terms. The important technical point to notice is that since the logarithmic terms appear in a definite integral, which involves the difference between the logarithmic functions at two integration limits, it will be meaningful when (i) the argument of logarithm is positive definite, or (ii) the argument of logarithm is negative definite. In the later case, an overall phase of π from the two ends cancels out. Requiring the argument of logarithm to be positive definite, or negative definite for $0 \leqslant \theta \leqslant 2\pi$ gives some constraints for the integration on k of each term of the above equation. Let us

denote the first (second) term of the above integral as R^+ (R^-). Then we can write

$$\begin{aligned}
R^+(\boldsymbol{q},\Omega) &= \frac{g\gamma^2}{4\pi^2\hbar^2 v_x^2}\int d\theta \int_0^{\mu/(1+\eta\cos(\theta+\phi))} kdk \frac{(\Omega+k)+k'm}{(\Omega+k)^2-(k')^2} \\
&= \frac{g\gamma^2}{4\pi^2\hbar^2 v_x^2}\int d\theta \left\{ \frac{\mu(\Omega+q\cos\theta)}{2(1+\eta\cos(\theta+\phi))(\Omega-q\cos\theta)} + \frac{\mu^2}{2(1+\eta\cos(\theta+\phi))^2(\Omega-q\cos\theta)} \right. \\
&\quad - \frac{\mu(\Omega^2-q^2)}{2(1+\eta\cos(\theta+\phi))(\Omega-q\cos\theta)^2} - (\Omega^2-q^2)\left(\frac{(\Omega+q\cos\theta)}{4(\Omega-q\cos\theta)^2} - \frac{(\Omega^2-q^2)}{4(\Omega-q\cos\theta)^3}\right) \\
&\quad \times \ln[K^+(\mu^+)]\Theta(q-\Omega)\Theta(\mu-\mu^+) - (\Omega^2-q^2)\left(\frac{(\Omega+q\cos\theta)}{4(\Omega-q\cos\theta)^2} - \frac{(\Omega^2-q^2)}{4(\Omega-q\cos\theta)^3}\right) \\
&\quad \left. \times \ln[K^+(\mu)](\Theta(\Omega-q)+\Theta(q-\Omega)\Theta(\mu^+-\mu)) \right\} \qquad \text{(B2)}
\end{aligned}$$

and

$$\begin{aligned}
R^-(\boldsymbol{q},\Omega) &= \frac{g\gamma^2}{4\pi^2\hbar^2 v_x^2}\int d\theta \int_0^{\mu/(1-\eta\cos(\theta+\phi))} kdk \frac{(-\Omega+k)+k'm}{(-\Omega+k)^2-(k')^2} \\
&= \frac{g\gamma^2}{4\pi^2\hbar^2 v_x^2}\int d\theta \left\{ \frac{\mu(\Omega-q\cos\theta)}{2(1-\eta\cos(\theta+\phi))(\Omega+q\cos\theta)} - \frac{\mu^2}{2(1-\eta\cos(\theta+\phi))^2(\Omega+q\cos\theta)} \right. \\
&\quad + \frac{\mu(\Omega^2-q^2)}{2(1-\eta\cos(\theta+\phi))(\Omega+q\cos\theta)^2} + (\Omega^2-q^2)\left(\frac{(\Omega-q\cos\theta)}{4(\Omega+q\cos\theta)^2} - \frac{(\Omega^2-q^2)}{4(\Omega+q\cos\theta)^3}\right)\ln[K^-(\mu_1^-)] \\
&\quad \times \Theta(\Omega-q)\Theta(\mu-\mu_1^-) + (\Omega^2-q^2)\left(\frac{(\Omega-q\cos\theta)}{4(\Omega+q\cos\theta)^2} - \frac{(\Omega^2-q^2)}{4(\Omega+q\cos\theta)^3}\right)\ln[K^-(\mu_2^-)]\Theta(q-\Omega)\Theta(\mu-\mu_2^-) \\
&\quad + (\Omega^2-q^2)\left(\frac{(\Omega-q\cos\theta)}{4(\Omega+q\cos\theta)^2} - \frac{(\Omega^2-q^2)}{4(\Omega+q\cos\theta)^3}\right)\ln[K^-(\mu)](\Theta(\Omega-q)\Theta(\mu_1^--\mu)+\Theta(q-\Omega)\Theta(\mu_2^- -\mu)) \\
&\quad \left. + (\Omega^2-q^2)\left(\frac{(\Omega-q\cos\theta)}{4(\Omega+q\cos\theta)^2} - \frac{(\Omega^2-q^2)}{4(\Omega+q\cos\theta)^3}\right)(\ln[K^-(\mu)]-\ln[K^-(\mu'^-)])\Theta(\Omega-q)\Theta(\mu-\mu'^-)\right\}, \qquad \text{(B3)}
\end{aligned}$$

where

$$K^+(\mu) = 1 + \frac{2\mu(\Omega-q\cos\theta)}{(1+\eta\cos(\theta+\phi))(\Omega^2-q^2)}, \qquad K^-(\mu) = 1 - \frac{2\mu(\Omega+q\cos\theta)}{(1-\eta\cos(\theta+\phi))(\Omega^2-q^2)}. \qquad \text{(B4)}$$

When the k integration runs up to the upper limit given in terms of μ, the argument of the log function given in Eq. (B4) might change sign. We need to cut the integral off once the sign change occurs. The sign changes from positive (negative) to negative (positive) occur at μ^+, μ_1^-, μ_2^- (μ'^-), where

$$\mu^+ = (q^2-\Omega^2)\frac{1+\eta\cos(\phi+\upsilon)}{2(\Omega-q\cos\upsilon)}, \qquad \upsilon = \arccos\left[\frac{\alpha\beta-\sqrt{\alpha^2\beta^2-(\beta^2+\zeta^2)(\alpha^2-\zeta^2)}}{(\zeta^2+\beta^2)}\right], \qquad \text{(B5)}$$

$$\mu_1^- = (\Omega^2-q^2)\frac{1-\eta\cos(\phi+\upsilon)}{2(\Omega+q\cos\upsilon)}, \qquad \upsilon = -\arccos\left[\frac{-\alpha\beta+\sqrt{\alpha^2\beta^2-(\beta^2+\zeta^2)(\alpha^2-\zeta^2)}}{(\zeta^2+\beta^2)}\right], \qquad \text{(B6)}$$

$$\mu_2^- = (\Omega^2-q^2)\frac{1-\eta\cos(\phi+\upsilon)}{2(\Omega+q\cos\upsilon)}, \qquad \upsilon = -\arccos\left[\frac{-\alpha\beta-\sqrt{\alpha^2\beta^2-(\beta^2+\zeta^2)(\alpha^2-\zeta^2)}}{(\zeta^2+\beta^2)}\right], \qquad \text{(B7)}$$

$$\mu'^- = (\Omega^2-q^2)\frac{1-\eta\cos(\phi+\upsilon)}{2(\Omega+q\cos\upsilon)}, \qquad \upsilon = \arccos\left[\frac{-\alpha\beta-\sqrt{\alpha^2\beta^2-(\beta^2+\zeta^2)(\alpha^2-\zeta^2)}}{(\zeta^2+\beta^2)}\right]. \qquad \text{(B8)}$$

Here, in the right-hand side of the above relations, $\zeta = q + \Omega\eta\cos\phi$, $\beta = \Omega\eta\sin\phi$, and $\alpha = q\eta\sin\phi$. The definitions of μ^+, μ_1^-, μ_2^- (μ'^-) are (is) such that the arguments $K^\pm$ of logarithm are always positive (negative) for every value of $0 < \theta < 2\pi$.

So far, we have done the integration on k. The next step is to do the angular integration. This can be basically done with the calculus of residues. This is straightforward for terms involving fractions of polynomials of trigonometric functions of θ. When we face the logarithmic function, one has to handle a branch cut. For this, the trick we use is to represent the logarithmic functions in terms of and integration over some auxiliary variable τ as

$$\ln(1+K) = \int_0^1 \frac{K\,d\tau}{1+\tau K}. \qquad \text{(B9)}$$

We use this representation and do the angular integration with the calculus of residues. At the end, we perform the integration on τ. We can summarize the final result for $R^{\pm}$ as a piecewise continuous function of the following form:

$$R^{+}(\boldsymbol{q},\Omega)=F^{0}(\boldsymbol{q},\Omega)+F^{1}(\boldsymbol{q},\Omega)\begin{cases}\Theta(\Omega-q), & G(X^{+}(\mu))|_{0}^{1}\\ \Theta(q-\Omega)\Theta(\mu^{+}-\mu), & G(X^{+}(\mu))|_{0}^{x_{u}^{+}(\mu)}\\ \Theta(q-\Omega)\Theta(\mu-\mu^{+}), & G(X^{+}(\mu^{+}))|_{0}^{x_{u}^{+}(\mu^{+})}\end{cases} \tag{B10}$$

and

$$R^{-}(\boldsymbol{q},\Omega)=F^{0}(\boldsymbol{q},\Omega)+F^{1}(\boldsymbol{q},\Omega)\begin{cases}\Theta(\Omega-q)\Theta(\mu_{1}^{-}-\mu), & G(X^{-}(\mu))|_{0}^{x_{u}^{-}(\mu)}\\ \Theta(q-\Omega)\Theta(\mu_{2}^{-}-\mu)), & G(X^{-}(\mu))|_{0}^{x_{u}^{-}(\mu)}\\ \Theta(\Omega-q)\Theta(\mu-\mu_{1}^{-}), & G(X^{-}(\mu_{-}^{1}))|_{0}^{x_{u}^{-}(\mu_{1}^{-})}\\ \Theta(q-\Omega)\Theta(\mu-\mu_{2}^{-}), & G(X^{-}(\mu_{-}^{2}))|_{0}^{x_{u}^{-}(\mu_{2}^{-})}\\ \Theta(\Omega-q)\Theta(\mu-\mu^{'-}), & G(X^{-}(\mu_{-}^{'}))|_{0}^{x_{u}^{-}(\mu^{'-})}\\ & +G(X^{-}(\mu))|_{0}^{x_{u}^{-}(\mu)}-G(X^{-}(\mu))|_{x_{d}^{-}(\mu)}^{1}\end{cases}. \tag{B11}$$

Using the above $R^{\pm}$, we can summarize $\mathrm{Re}\Delta\chi$ as

$$\Re\Delta\chi(\boldsymbol{q},\Omega)=F^{0}(\boldsymbol{q},\Omega)+F^{1}(\boldsymbol{q},\Omega)\left(G(X^{+})|_{x_{d}^{+}}^{x_{u}^{+}}+\sum G(X^{-})|_{x_{d}^{-}}^{x_{u}^{-}}\right), \tag{B12}$$

where the $\pm$ in $X^{\pm}$ points to the $R^{\pm}$. The summation $\sum$ in $G(X^{-})$ indicates that in the last piece of Eq. (B11) we have three different regions contributing to the integral. The functions F^{0}, F^{1}, and G are given by

$$F^{0}(\boldsymbol{q},\Omega)=\frac{g}{16\pi\hbar^{2}v_{x}v_{y}}\frac{\mu\,q^{2}}{\sqrt{1-\eta^{2}}}\frac{A(\boldsymbol{q},\Omega)}{D^{2}(\boldsymbol{q},\Omega)}, \tag{B13}$$

$$F^{1}(\boldsymbol{q},\Omega)=\frac{g}{16\pi\hbar^{2}v_{x}v_{y}}\frac{q^{2}}{\sqrt{|\Omega^{2}-q^{2}|}}, \tag{B14}$$

$$G(x)=B(\boldsymbol{q},\Omega)x\sqrt{x^{2}-x'}-\mathrm{sgn}(\Omega-q)\cosh^{-1}\frac{x}{x'}, \tag{B15}$$

where $\mathrm{sgn}(\Omega-q)$ is the sign function. The coefficient $A(\boldsymbol{q},\Omega)$, $B(\boldsymbol{q},\Omega)$, $D(\boldsymbol{q},\Omega)$, and $X^{\lambda=\pm}$ have the following definitions:

$$\begin{aligned}&A(\boldsymbol{q},\Omega)=q^{2}(\eta^{4}+8\eta^{2}-8)+4\eta^{4}\Omega^{2}4q\eta\Omega\cos\phi(5\eta^{2}-4)+4\eta^{2}\Omega^{2}(\eta^{2}-1)\cos2\phi-q\eta^{3}(4\Omega\cos3\phi+q\eta\cos4\phi),\\ &B(\boldsymbol{q},\Omega)=((q+\eta\Omega\cos\phi)^{2}-\eta^{2}(\Omega^{2}-q^{2})\sin^{2}\phi)/D^{2}(\boldsymbol{q},\Omega),\quad D(q,\Omega)=(q+\eta\Omega\cos\phi)^{2}+\eta^{2}(\Omega^{2}-q^{2})\sin^{2}\phi,\end{aligned} \tag{B16}$$

$$X^{\lambda}=2\tilde{\mu}x+\lambda(\Omega+q\eta\cos\phi),\quad x'=(\Omega+q\eta\cos\phi)^{2}-(1-\eta^{2})(\Omega^{2}-q^{2}), \tag{B17}$$

$$x_{u(d)}^{-}=\frac{1}{2\mu}((\Omega+q\eta\cos\phi)-(+)\sqrt{x'}),\quad x_{u}^{+}=-\frac{1}{2\mu}((\Omega+q\eta\cos\phi)+\sqrt{x'}). \tag{B18}$$

Here, $\tilde{\mu}$ represents either of μ^{+}, μ_{1}^{-}, μ_{2}^{-}, $\mu^{'-}$, depending on which piece of the $R^{\pm}$ functions in Eqs. (B10) and (B11) supports the value of $\mathrm{Re}\Delta\chi$. The above results are benchmarked in Fig. 2 against the numerical results of Ref. [34] (where the real part is numerically obtained by using Kramers-Kronig relation).

2. Imaginary part

In order to calculate the imaginary part, we start from Eq. (B1) and use $\Im[1/(x+i\epsilon)]=-\pi\delta(x)$ to write

$$\begin{aligned}\Im\Delta\chi(\boldsymbol{q},\Omega)=-\frac{g\pi\gamma^{2}}{2A\hbar^{2}v_{x}^{2}}\sum_{\boldsymbol{k}}&\Theta(\mu-k-k\eta\cos\theta_{k})((1+\cos(\theta_{k}-\theta_{k'}))\delta(\Omega+k-k')+(1-\cos(\theta_{k}-\theta_{k'}))\delta(\Omega+k+k'))\\ &-\Theta(\mu-k+k\eta\cos\theta_{k})((1+\cos(\theta_{k}-\theta_{k'}))\delta(-\Omega+k-k')+(1-\cos(\theta_{k}-\theta_{k'}))\delta(-\Omega+k+k')).\end{aligned} \tag{B19}$$

We only need to evaluate the above function for positive Ω, and the negative Ω results can be obtained by appropriate symmetry relations. This assumption makes the second term in the above relation irrelevant as the Dirac delta function does not pick any

pole. Therefore we are left with the positive Ω contribution from the first term that splits into three parts:

$$
\begin{aligned}
I_1(\boldsymbol{q},\Omega) &= -\frac{g\gamma^2}{8\pi\hbar^2 v_x^2}\int d\boldsymbol{k}\Theta(\mu-k-k\eta\cos\theta)(1+\cos(\theta_k-\theta_{k'}))\delta(\Omega+k-k'),\\
I_2(\boldsymbol{q},\Omega) &= \frac{g\gamma^2}{8\pi\hbar^2 v_x^2}\int d\boldsymbol{k}\Theta(\mu-k+k\eta\cos\theta)(1+\cos(\theta_k-\theta_{k'}))\delta(-\Omega+k-k'),\\
I_3(\boldsymbol{q},\Omega) &= \frac{g\gamma^2}{8\pi\hbar^2 v_x^2}\int d\boldsymbol{k}\Theta(\mu-k+k\eta\cos\theta)(1+\cos(\theta_k-\theta_{k'}))\delta(-\Omega+k+k').
\end{aligned}
\tag{B20}
$$

By change of variable $\theta\to\theta+\phi$ and using $\delta[f(z)]=\delta(z-z_0)/|f'(z_0)|$, we rewrite the delta functions as $\delta(\theta-\theta_0)/|kq\sin\theta_0|$. In this equation, the $\cos\theta_0$ for each delta function has its own definition, and obviously $\sin\theta_0=\pm\sqrt{1-\cos^2\theta_0}$. The trigonometric inequality $-1\leqslant\cos\theta_0\leqslant 1$ places some constraints on the q and Ω as follows:

$$
\begin{aligned}
\delta(\Omega+k-k'):&\quad \cos\theta_0=(\Omega^2+2\Omega k-q^2)/2kq,\quad \Omega+2k>q\\
\delta(-\Omega+k-k'):&\quad \cos\theta_0=(\Omega^2-2\Omega k-q^2)/2kq,\quad -\Omega+2k>q\\
\delta(-\Omega+k+k'):&\quad \cos\theta_0=(\Omega^2-2\Omega k-q^2)/2kq,\quad \Omega-q<2k<\Omega+q.
\end{aligned}
\tag{B21}
$$

With the above expressions for $\cos\theta_0$ and $\sin\theta_0$, the above three integrals can be evaluated to give

$$
\begin{aligned}
I_1(\boldsymbol{q},\Omega) &= -\frac{g\gamma^2}{32\pi\hbar^2 v_x^2}\frac{q^2}{\sqrt{q^2-\Omega^2}}\Theta(q-\Omega)\int_1^\infty dp\sqrt{p^2-1}\,\Theta(a^+(\boldsymbol{q},\Omega)-b^+(\boldsymbol{q},\Omega)p\pm c^+(\boldsymbol{q},\omega)\sqrt{p^2-1})\\
&= -\frac{g\gamma^2}{32\pi\hbar^2 v_x^2}\frac{q^2}{\sqrt{q^2-\Omega^2}}\Theta(q-\Omega)\big\{\Theta(a^+(\boldsymbol{q},\Omega)+b^+(\boldsymbol{q},\Omega))\big(G_0^+(x)\big|_1^{r_1^+}+G_0^+(x)\big|_1^{r_2^+}\big)\\
&\quad+\Theta(-a^+(\boldsymbol{q},\Omega)-b^+(\boldsymbol{q},\Omega))\Theta(a^+(\boldsymbol{q},\Omega)^2-b^+(\boldsymbol{q},\Omega)^2+c^+(\boldsymbol{q},\Omega)^2)G_0^+(x)\big|_{r_1^+}^{r_2^+}\big\},
\end{aligned}
\tag{B22}
$$

$$
\begin{aligned}
I_2(\boldsymbol{q},\Omega) &= \frac{g\gamma^2}{32\pi\hbar^2 v_x^2}\frac{q^2}{\sqrt{q^2-\Omega^2}}\Theta(q-\Omega)\int_1^\infty dp\sqrt{p^2-1}\,\Theta(a^-(\boldsymbol{q},\Omega)-b^-(\boldsymbol{q},\Omega)p\pm c^-(\boldsymbol{q},\omega)\sqrt{p^2-1})\\
&= \frac{g\gamma^2}{32\pi\hbar^2 v_x^2}\frac{q^2}{\sqrt{q^2-\Omega^2}}\Theta(q-\Omega)\big\{\Theta(a^-(\boldsymbol{q},\Omega)+b^-(\boldsymbol{q},\Omega))\big(G_0^+(x)\big|_1^{r_1^-}+G_0^+(x)\big|_1^{r_2^-}\big)\\
&\quad+\Theta(-a^-(\boldsymbol{q},\Omega)-b^-(\boldsymbol{q},\Omega))\Theta(a^-(\boldsymbol{q},\Omega)^2-b^-(\boldsymbol{q},\Omega)^2+c^-(\boldsymbol{q},\Omega)^2)G_0^+(x)\big|_{r_1^-}^{r_2^-}\big\},
\end{aligned}
\tag{B23}
$$

$$
\begin{aligned}
I_3(\boldsymbol{q},\Omega) &= \frac{g\gamma^2}{32\pi\hbar^2 v_x^2}\frac{q^2}{\sqrt{\Omega^2-q^2}}\Theta(\Omega-q)\int_{-1}^1 dp\sqrt{1-p^2}\,\Theta(a^-(\boldsymbol{q},\Omega)-b^-(\boldsymbol{q},\Omega)p\pm c^-(\boldsymbol{q},\omega)\sqrt{p^2-1})\\
&= \frac{g\gamma^2}{32\pi\hbar^2 v_x^2}\frac{q^2}{\sqrt{\Omega^2-q^2}}\Theta(\Omega-q)\big\{2\Theta(a^-(\boldsymbol{q},\Omega)+b^-(\boldsymbol{q},\Omega))G_0^-(x)\big|_{-1}^1\\
&\quad+\Theta(a^-(\boldsymbol{q},\Omega)+b^-(\boldsymbol{q},\Omega))\Theta(\Delta^-(\boldsymbol{q},\Omega))\Theta(1-|u(\boldsymbol{q},\Omega)|)\big(G_0^-(x)\big|_{-1}^{r_1^-}+G_0^-(x)\big|_{-1}^{r_2^-}\big)\\
&\quad+\Theta(a^-(\boldsymbol{q},\Omega)+b^-(\boldsymbol{q},\Omega))\Theta(\Delta^-(\boldsymbol{q},\Omega))\Theta(-1-u(\boldsymbol{q},\Omega))G_0^-(x)\big|_{r_1^-}^{r_2^-}\\
&\quad-\Theta(-a^-(\boldsymbol{q},\Omega)-b^-(\boldsymbol{q},\Omega))\Theta(\Delta^-(\boldsymbol{q},\Omega))\Theta(|u(\boldsymbol{q},\Omega)|-1)G_0^-(x)\big|_{r_1^-}^{r_2^-}\\
&\quad+\Theta(-a^-(\boldsymbol{q},\Omega)-b^-(\boldsymbol{q},\Omega))\Theta(\Delta^-(\boldsymbol{q},\Omega))\Theta(1-|u(\boldsymbol{q},\Omega)|)\big(G_0^-(x)\big|_{-1}^{r_2^-}+G_0^-(x)\big|_{-1}^{r_2^-}\big)\big\},
\end{aligned}
\tag{B24}
$$

In above equations, $p=(2k\pm\Omega)/q$, where $+$ stands for I_1 and $-$ stands for I_2, I_3. The definition of functions used in the above relations is given by

$$
G_0^+(x)=x\sqrt{x^2-1}-\cosh^{-1}(x),\quad G_0^-(x)=x\sqrt{1-x^2}+\sin^{-1}(x),
\tag{B25}
$$

$$
r_{1(2)}^\lambda=\frac{-a^\lambda(\boldsymbol{q},\Omega)b^\lambda(\boldsymbol{q},\Omega)-(+)c^\lambda(\boldsymbol{q},\Omega)+\lambda\sqrt{\Delta^\lambda(\boldsymbol{q},\Omega)}}{(b^\lambda(\boldsymbol{q},\Omega))^2-(c^\lambda(\boldsymbol{q},\Omega))^2},\quad \Delta^\lambda(\boldsymbol{q},\Omega)=(a^\lambda(\boldsymbol{q},\Omega))^2-(b^\lambda(\boldsymbol{q},\Omega))^2+(c^\lambda(\boldsymbol{q},\Omega))^2,
\tag{B26}
$$

where $\lambda = \pm$ and

$$a^{\pm}(\boldsymbol{q}, \Omega) = 2\mu \pm \Omega \pm q\eta\cos\phi, \quad b^{\lambda}(\boldsymbol{q}, \Omega) = -(q + \Omega\eta\cos\phi),$$
$$c^{\lambda}(\boldsymbol{q}, \Omega) = \lambda\eta\sin\phi\sqrt{|q^2 - \Omega^2|}, \quad u(\boldsymbol{q}, \Omega) = \frac{a^{-}(\boldsymbol{q}, \Omega)}{b(\boldsymbol{q}, \Omega)}. \tag{B27}$$

[1] T. O. Wehling, A. M. Black-Schaffer, and A. V. Balatsky, Adv. Phys. **63**, 1 (2014).
[2] E. Fradkin, *Field Theories of Condensed Matter Physics* (Cambridge University Press, New York, 2013).
[3] K. S. Novoselov, A. K. Geim, S. V. Morozov, D. Jiang, Y. Zhang, S. V. Dubonos, I. V. Grigorieva, and A. A. Firsov, Science **306**, 666 (2004).
[4] N. P. Armitage, E. J. Mele, and A. Vishwanath, Rev. Mod. Phys. **90**, 015001 (2018).
[5] Y. Fuseya, M. Ogata, and H. Fukuyama, J. Phys. Soc. Jpn. **84**, 012001 (2015).
[6] A. Bostwick, T. Ohta, T. Seyller, K. Horn, and E. Rotenberg, Nat. Phys. **3**, 36 (2007).
[7] A. H. Castro Neto, F. Guinea, N. M. R. Peres, K. S. Novoselov, and A. K. Geim, Rev. Mod. Phys. **81**, 109 (2009).
[8] S. Das Sarma, S. Adam, E. H. Hwang, and E. Rossi, Rev. Mod. Phys. **83**, 407 (2011).
[9] V. Georgakilas, M. Otyepka, A. B. Bourlinos, V. Chandra, N. Kim, K. C. Kemp, P. Hobza, R. Zboril, and K. S. Kim, Chem. Rev. **112**, 6156 (2012).
[10] S.-M. Choi, S.-H. Jhi, and Y.-W. Son, Phys. Rev. B **81**, 081407 (2010).
[11] C. Si, Z. Sun, and F. Liu, Nanoscale **8**, 3207 (2016).
[12] D. C. Cabra, N. E. Grandi, G. A. Silva, and M. B. Sturla, Phys. Rev. B **88**, 045126 (2013).
[13] S. Katayama, A. Kobayashi, and Y. Suzumura, J. Phys. Soc. Jpn. **75**, 054705 (2006).
[14] N. Tajima, S. Sugawara, M. Tamura, Y. Nishio, and K. Kajita, J. Phys. Soc. Jpn. **75**, 051010 (2006).
[15] K. Kajita, Y. Nishio, N. Tajima, Y. Suzumura, and A. Kobayashi, J. Phys. Soc. Jpn. **83**, 072002 (2014).
[16] M. O. Goerbig, J.-N. Fuchs, G. Montambaux, and F. Piéchon, Phys. Rev. B **78**, 045415 (2008).
[17] S. Katayama, A. Kobayashi, and Y. Suzumura, Eur. Phys. J. B **67**, 139 (2009).
[18] J. Sári, C. Tőke, and M. O. Goerbig, Phys. Rev. B **90**, 155446 (2014).
[19] A. Kobayashi, S. Katayama, and Y. Suzumura, Sci. Technol. Adv. Mater. **10**, 024309 (2009).
[20] H. Kino and T. Miyazaki, J. Phys. Soc. Jpn. **75**, 034704 (2006).
[21] A. Kobayashi, S. Katayama, Y. Suzumura, and H. Fukuyama, J. Phys. Soc. Jpn. **76**, 034711 (2007).
[22] M. K. S. Ishibashi, T. Tamura, and K. Terakura, J. Phys. Soc. Jpn. **75**, 015005 (2006).
[23] P. Alemany, J.-P. Pouget, and E. Canadell, Phys. Rev. B **85**, 195118 (2012).
[24] Y. Mao, W. L. Wang, D. Wei, E. Kaxiras, and J. G. Sodroski, ACS Nano **5**, 1395 (2011).
[25] X.-F. Zhou, X. Dong, A. R. Oganov, Q. Zhu, Y. Tian, and H.-T. Wang, Phys. Rev. Lett. **112**, 085502 (2014).
[26] A. Lopez-Bezanilla and P. B. Littlewood, Phys. Rev. B **93**, 241405 (2016).
[27] B. Feng, O. Sugino, R.-Y. Liu, J. Zhang, R. Yukawa, M. Kawamura, T. Iimori, H. Kim, Y. Hasegawa, H. Li, L. Chen, K. Wu, H. Kumigashira, F. Komori, T.-C. Chiang, S. Meng, and I. Matsuda, Phys. Rev. Lett. **118**, 096401 (2017).
[28] B. Commeau, R. M. Geilhufe, G. W. Fernando, and A. V. Balatsky, Phys. Rev. B **96**, 125135 (2017).
[29] A. J. Mannix, X.-F. Zhou, B. Kiraly, J. D. Wood, D. Alducin, B. D. Myers, X. Liu, B. L. Fisher, U. Santiago, J. R. Guest, M. J. Yacaman, A. Ponce, A. R. Oganov, M. C. Hersam, and N. P. Guisinger, Science **350**, 1513 (2015).
[30] A. D. Zabolotskiy and Y. E. Lozovik, Phys. Rev. B **94**, 165403 (2016).
[31] T. S. Sikkenk and L. Fritz, Phys. Rev. B **96**, 155121 (2017).
[32] E. H. Hwang and S. Das Sarma, Phys. Rev. B **75**, 205418 (2007).
[33] T. B. Wunsch, Stauber, F. Sols, and F. Guinea, New J. Phys. **8**, 318 (2006).
[34] T. Nishine, A. Kobayashi, and Y. Suzumura, J. Phys. Soc. Jpn. **79**, 114715 (2010).
[35] K. Sadhukhan and A. Agarwal, Phys. Rev. B **96**, 035410 (2017).
[36] T. Nagao, T. Hildebrandt, M. Henzler, and S. Hasegawa, Phys. Rev. Lett. **86**, 5747 (2001).
[37] T. Morinari, T. Himura, and T. Tohyama, J. Phys. Soc. Jpn. **78**, 023704 (2009).
[38] S. Katayama, A. Kobayashi, and Y. Suzumura, J. Phys.: Conf. Ser. **132**, 012003 (2008).
[39] P. Phillips, *Advanced Solid State Physics* (Cambridge University Press, New York, 2012).
[40] D. Bohm and D. Pines, Phys. Rev. **92**, 609 (1953).
[41] A. L. Fetter, Ann. Phys. **81**, 367 (1973).
[42] Z. Jalali-Mola and S. A. Jafari, J. Magn. Magn. Mater. **471**, 220 (2019).
[43] S. Verma, A. Mawrie, and T. K. Ghosh, Phys. Rev. B **96**, 155418 (2017).
[44] M. I. Katsnelson, *Graphene: Carbon in Two Dimension* (Cambridge University Press, New York, 2012).
[45] M. E. Peskin and D. V. Schroeder, *An Introduction To Quantum Field Theory* (Addison-Wesley, Reading, USA, 1995).
[46] G. B. Arfken, H. J. Weber, and F. E. Harris, *Mathematical Methods for Physicists* (Academic Press, Boston, 2013).